Journal of Materials Chemistry A

PAPER

View Article Online
View Journal | View Issue

Cite this: J. Mater. Chem. A, 2017, 5, 11236

General solution-processed formation of porous transition-metal oxides on exfoliated molybdenum disulfides for high-performance asymmetric supercapacitors†

Kai Wang,[a] Jing Yang,[a] Jixin Zhu,[b] Le Li,[a] Ying Liu,[a] Chao Zhang *[a] and Tianxi Liu *[a]

Received 16th February 2017
Accepted 10th May 2017

DOI: 10.1039/c7ta01457k

rsc.li/materials-a

The combination of hierarchical porous transition-metal oxides with ultrathin two-dimensional (2D) transition-metal dichalcogenides (TMDs) with a favorable electrochemical performance beyond single-component materials is still very challenging. The present work demonstrates the general and targeted synthesis of hybrid heterostructures by the integration of porous transition-metal oxides (TMOs, *e.g.* NiO, Co_3O_4 and Fe_2O_3) and 2D MoS_2 nanosheets. The as-prepared vertically aligned MoS_2–NiO hybrids exhibit an excellent pseudocapacitive performance, such as a high specific capacitance of 1080.6 at 1 A g^{-1} and long cycling durability with 101.9% capacitance retention after 9000 cycles at 2 A g^{-1}. This facile strategy using low-cost precursors is regarded as a general method to hybridize 2D MoS_2 with other porous TMOs, such as Co_3O_4 and Fe_2O_3, with largely improved pseudocapacitive performances due to a favorable synergistic effect between MoS_2 and TMOs with an enhanced electronic/ionic transport. Asymmetric supercapacitors using MoS_2–TMO hybrids as both positive and negative electrodes are also demonstrated. As a proof-of-concept, the as-assembled MoS_2–NiO//MoS_2–Fe_2O_3 asymmetric supercapacitor operating within the potential window of 0–1.8 V delivers a high energy density of 39.6 W h kg^{-1} with a long cycle life and excellent rate capability.

Introduction

Supercapacitors, which store charges through either ion adsorptions (electric double-layer capacitive behavior) or fast reversible redox reactions (pseudocapacitive behavior), have been considered as advanced energy storage devices, and thus attracted tremendous interest due to their high power density, ultrafast charge and discharge rates, and long cycle life.[1] However, the dramatically increasing demands in portable electronic devices and hybrid electric vehicles have propelled the supercapacitors from the state-of-the-art into next-generation energy storage systems with stronger specific power, higher specific energy, and longer lifespan.[2] Electrode materials based on transition metal oxides/hydroxides such as RuO_2,[3,4] Co_3O_4,[5,6] $Co(OH)_2$,[2,7] NiO,[8,9] $Ni(OH)_2$ (ref. 10) and $NiCo_2O_4$ (ref. 11) are currently at the forefront of various emerging electrode materials for supercapacitors owing to their large specific capacitances and fast redox kinetics. Particularly, due to their environmental friendliness, chemical stability, natural abundance and high theoretical capacitance, nickel, cobalt and iron-based oxides can be exploited as promising electrode material candidates replacing hydrous RuO_2.[12–14] Nevertheless, these nickel, cobalt and iron-based oxides normally exhibit a low surface area and poor electrical conductivity, which lead to high internal resistances and thus limit ion/electron transfer rates for high-performance supercapacitors. Therefore, it is still a great challenge to develop high-performance electrode materials using transition metal oxides (TMOs) with large energy storage performance associated with high rate capability.[15–18]

Heterostructures made by atomic-scale stacking of different nanostructures (especially van der Waals heterostructures) are a new class of materials with fascinating properties.[19,20] In order to maximize the intrinsic properties of TMOs, it is vital to design and build TMO-based heterostructures to promote the electrochemical activity of the as-synthesized TMO-based electrode materials.[21,22] The heterostructure can create an abundance of structural defects and multiple accessible electrochemically active sites for ion/electron migrations, which would largely

[a]State Key Laboratory for Modification of Chemical Fibers and Polymer Materials, College of Materials Science and Engineering, Donghua University, Shanghai 201620, P. R. China. E-mail: czhang@dhu.edu.cn; txliu@fudan.edu.cn; txliu@dhu.edu.cn; Fax: +86-21-67874062; Tel: +86-21-67874060

[b]Key Laboratory of Flexible Electronics (KLOFE), Institute of Advanced Materials (IAM), Jiangsu National Synergetic Innovation Center for Advanced Materials (SICAM), Nanjing Tech University (NanjingTech), 30 South Puzu Road, Nanjing 211816, China

† Electronic supplementary information (ESI) available: Fig. S1–S26, Tables S1 and S2. See DOI: 10.1039/c7ta01457k

enhance the redox reaction activities towards electrochemical energy storage.[23] Molybdenum disulfide (MoS_2), as a typical transition-metal dichalcogenide (TMD), possesses a unique two-dimensional (2D) structure but exhibits superior electronic properties and significantly lower energy dissipation than 2D graphene.[24] Unique physical and chemical properties can be acquired when MoS_2 is in the form of single and few layers upon exfoliation.[25–28] The lateral similarity of MoS_2 and TMOs provides a high possibility to fabricate a heterostructure composed of MoS_2 and TMOs, which is regarded as an efficient approach to obtain a unique heterostructure that simultaneously exhibits prominent electric double-layer capacitive and pseudocapacitive performances. Therefore, the design and fabrication of MoS_2 with TMOs into an integrated heterostructure would be expected to be promising electrode materials for supercapacitors due to their large theoretical capacitance, enlarged electroactive surface area and rich redox reactions.[29–33]

Herein, we report a facile and general strategy to tackle the challenges for the decoration of few-layered MoS_2 (f-MoS_2) with a series of TMOs (Ni, Co, and Fe-based oxides) *via* a chemical bath deposition method under ambient conditions. Remarkably, this solution-processed growth method shows the versatility and feasibility for obtaining heterostructured MoS_2–TMO hybrids with tunable morphologies and compositions. These unique and novel nanostructured MoS_2–TMO hybrids are expected to have many merits: (1) a general and green approach has been adopted to fabricate these MoS_2–TMO heterostructures with tunable morphologies. (2) Due to the size confinements of enhanced electron–electron interactions,[33–35] MoS_2–TMO heterostructures with good ion permeability and abundant surface active sites not only weaken the re-stacking of 2D MoS_2 and decorated TMOs themselves, but also ensure superior energy storage performance of such heterostructures in terms of large specific capacitances, excellent rate capacitances, and good cycling stabilities. (3) High energy density and durable asymmetric supercapacitors can be assembled using MoS_2–NiO or MoS_2–Co_3O_4 as positive electrode materials and MoS_2–Fe_2O_3 as the negative electrode material, which exhibit a wide potential window of 0–2.0 V and a high energy density of 39.6 W h kg^{-1}, demonstrating its potential applications in high-performance energy storage devices. (4) This scalable strategy thus highlights a rational design and efficient synthesis of low-cost and heterostructured TMO- and TMD-based materials, which can be widely utilized to prepare other TMO-based heterostructures for various applications, such as fuel cells, Li-ion batteries, catalysts and sensors.

Experimental

Materials

Bulk MoS_2 (b-MoS_2, ~325 meshes) was purchased from Alfa Aesar. Nickel nitrate hexahydrate ($Ni(NO_3)_2 \cdot 6H_2O$), cobalt nitrate hexahydrate ($Co(NO_3)_2 \cdot 6H_2O$), iron nitrate nonahydrate ($Fe(NO_3)_3 \cdot 9H_2O$), ammonia water (25–28%), *N*-methyl-2-pyrrolidone (NMP) and ethanol were supplied by Sinopharm Chemical Reagent. Deionized (DI) water was used throughout the experiments.

Preparation of few-layered MoS_2 (f-MoS_2)

A uniform dispersion of f-MoS_2 in water was obtained by a solvent-exchange method. Firstly, a uniform dispersion of f-MoS_2 in NMP was achieved *via* a sonication-assisted exfoliation of b-MoS_2.[36] Typically, 1.5 g b-MoS_2 powder was added into 200 mL of NMP with a sonication bath for 8 h. After that, the dark green suspension was centrifuged at 2000 rpm for 15 min, and the sediment was discarded to remove un-exfoliated or thicker MoS_2 flakes. Secondly, the supernatants were filtered, washed with ethanol and water several times successively, and then re-dispersed into DI water under sonication. The final concentration of f-MoS_2 in water was determined by a weighing method. In contrast, it is basically impossible to directly exfoliate a totally dried f-MoS_2 sediment or b-MoS_2 in water even by a long-time sonication (up to 200 h).

General synthesis of the MoS_2–TMO hybrids

Heterostructured MoS_2–TMO hybrids were synthesized by a CBD process followed by a post-annealing treatment in nitrogen. In a typical procedure, a certain amount of metal nitrite was added into 50 mL aqueous dispersion of 40 mg f-MoS_2, and then 50 mL aqueous ammonia (25–28%) was added under vigorous stirring. After being heated at 90 °C for 5 h, the suspension was filtered and rinsed with DI water and ethanol successively, and then the resultant solid was dried at 60 °C in a vacuum overnight, thus to obtain the MoS_2–TMO hybrids. In particular, the contents of TMO within the MoS_2–TMO hybrids were tuned by simply adjusting the feeding molar ratios of metal nitrite to f-MoS_2 of 4 : 1, 8 : 1 and 16 : 1. Accordingly, the as-prepared hybrids were named MoS_2–NiO-1, MoS_2–NiO-2 and MoS_2–NiO-3 for convenience. For comparison, neat TMO was prepared by a similar preparation procedure without the f-MoS_2 template.

Characterization

The morphology of all samples was evaluated by field-emission scanning electron microscopy (FESEM, Ultra 55) and transmission electron microscopy (TEM, Tecnai G2 20 TWIN). X-ray diffraction (XRD) patterns were obtained using an X'Pert Pro X-ray diffractometer with Cu K_α radiation at a current of 40 mA and voltage of 40 kV. Raman spectra were recorded on a Renishaw in plus laser Raman spectrometer with λ_{exc} = 532 nm.

Electrochemical characterization

The electrochemical capacitive behaviors of all samples were studied with a CHI 660D electrochemical workstation using a standard three-electrode setup. The working electrodes were prepared by mixing 80 wt% active materials, 10 wt% carbon black (Super P), and 10 wt% polyvinylidene fluoride (PVDF) in *N*-methyl-2-pyrrolidone (NMP) solution, followed by drying it on a graphite paper current collector (1 × 1 cm^2) in a vacuum at 80 °C. The typical loading density for the as-prepared electrodes is approximately ~1.0 mg cm^{-2}. A platinum wire and mercuric oxide electrode (Hg/HgO) were used as the counter electrode

and the reference electrode, respectively, and a 6.0 M KOH solution was employed as the electrolyte. Cycling voltammetry (CV) curves were measured within pre-set potential ranges at the scan rates of 5–200 mV s^{-1}. Galvanostatic charge/discharge testing was conducted at pre-set potential ranges at a current density of 0.5, 1, 2, 5, 10, 15 and 20 A g^{-1}, respectively. The electrochemically active surface area (ECSA) of the samples was measured by conducting CV scans from 0 to 0.1 V (the voltage range with no faradaic process) at the scan rates (ν) of 5, 10, 25, 50, 75 and 100 mV s^{-1}. The charging current (Δj) at 0.05 V was equal to the ν multiplied with the electrochemical double-layer capacitance (C_{dl}). Thus, the slope yielded by the straight line plotted for the relationship between Δj and ν indicated the C_{dl}. The ECSA was calculated by dividing the C_{dl} by the specific capacitance, C_s. The roughness factor (RF) was determined from the ratio of ECSA to the geometric area of the electrode (1 cm^2). Electrochemical impedance spectroscopy (EIS) was performed in the frequency range from 0.01 to 10^6 Hz at an open circuit potential with an AC voltage amplitude of 5 mV. Prior to the assembly of ASC devices, the mass ratio of the positive and negative electrode materials should follow the following equation:

$$\frac{m_+}{m_-} = \frac{C_- \times \Delta E_-}{C_+ \times \Delta E_+}$$

where C_+ and C_- are the specific capacitances of the positive and negative electrode materials, respectively, ΔE_- and ΔE_+ represent the potential windows, and m_+ and m_- are the masses of the positive and negative electrode materials, respectively.

Results and discussion

Fig. 1 demonstrates the schematic of general preparation of MoS_2–TMO (*i.e.* NiO, Co_3O_4, and Fe_2O_3) hybrids. As demonstrated in Fig. 1a, the liquid-phase exfoliation of bulk MoS_2 (b-MoS_2) in *N*-methyl-2-pyrrolidone (NMP) produces high-concentration and uniform dispersions of few-layered MoS_2 (f-MoS_2) (see Fig. S1a, ESI†).[37] Upon filtration, a sonication of wet-state f-MoS_2 produces uniform aqueous dispersions of f-MoS_2 (see Fig. S1b, ESI†). The scalable solvent-exchange strategy enables the achievement of full exfoliation and uniform aqueous dispersion of f-MoS_2, which facilitates the subsequent growth of TMOs on 2D MoS_2 through an easy solution-processed method. We also directly sonicate b-MoS_2 in water, but find that almost all MoS_2 particles quickly aggregate without exfoliation (Fig. S2, ESI†). The dispersion mechanism for why the f-MoS_2 aqueous dispersions are stable is also discussed. Indeed, we find that the properties of solvents for maintaining stable dispersions of MoS_2 are not inevitably the same as solvents used for an initial exfoliation.[38] When the flake sizes of MoS_2 remarkably decrease upon sonication, the amounts of edge S atoms sharply increase.[39,40] The resultant f-MoS_2 can easily get charged due to ionizations of edge-attached groups, which result in electrostatic repulsion between nanoflakes and further improve its dispersibility.[41]

Fig. 1 (a) Schematic illustration of the solvent-exchange strategy for preparing water dispersible f-MoS_2 nanosheets. (b) Schematic illustration of the general synthesis of porous NiO on f-MoS_2 nanosheets.

2D f-MoS_2 is further employed for growing porous nickel oxide (NiO) nanosheets, thus forming vertically aligned MoS_2–NiO hybrids. As shown in Fig. 1b, we get hybrid materials of nickel hydroxide ($Ni(OH)_2$) and MoS_2 by means of an easily processed chemical bath decomposition method. Then, by a post-annealing treatment, porous NiO within the MoS_2–NiO hybrids forms due to the decomposition of $Ni(OH)_2$ lamellae. The structural evolutions of $Ni(OH)_2$ to NiO during calcination are investigated by the nitrogen adsorption/desorption isotherms, as shown in Fig. S3 (ESI†) and summarized in Tables 1 and S1 (ESI†). NiO and MoS_2–NiO exhibit H4 type hysteresis loops. The Brunauer–Emmett–Teller (BET) surface area of NiO is ~86.8 m^2 g^{-1}, which is much larger than that of $Ni(OH)_2$ (~39.9 m^2 g^{-1}), indicating that more porosities are introduced when $Ni(OH)_2$ converts into NiO. The pore size distributions indicate that an extra micropore volume originates from NiO interlamellar spacing. Compared with $Ni(OH)_2$ and f-MoS_2, MoS_2–$Ni(OH)_2$ hybrids show a larger BET surface area of ~45.6 m^2 g^{-1} than those of f-MoS_2 (~36.4 m^2 g^{-1}) and $Ni(OH)_2$ (~39.9 m^2 g^{-1}). The enlarged pore volume of MoS_2–$Ni(OH)_2$ also indicates that f-MoS_2 functions as an ideal template for growing NiO.

The crystallographic structures for MoS_2–$Ni(OH)_2$ and MoS_2–NiO are determined by the X-ray diffraction (XRD) measurements (Fig. 2a and S4 in the ESI†). As shown in Fig. 2a, all the peaks of f-MoS_2 can be indexed to the hexagonal structure of 2H-phase MoS_2 (JCPDS card No. 65-1951). Compared with b-MoS_2 (Fig. S4a, ESI†), f-MoS_2 shows a relatively broadened primary (002) diffraction peak, demonstrating that more defects

Table 1 The BET surface areas and pore size distributions of MoS_2–NiO, f-MoS_2 and NiO

Samples	S_{BET} [m^2 g^{-1}]	Total pore volume [mL g^{-1}]	Micropore volume [mL g^{-1}]	Mesopore volume [mL g^{-1}]
f-MoS_2	36.4	0.12	~0	0.12
NiO	86.8	0.12	0.06	0.06
MoS_2–NiO	136.6	0.24	0.02	0.22

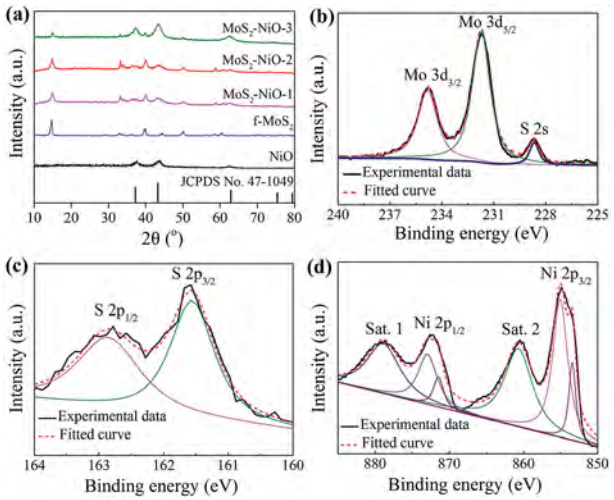

Fig. 2 (a) XRD patterns of MoS_2–NiO hybrids, NiO and f-MoS_2. High-resolution (b) Mo 3d, (c) S 2p and (d) Ni 2p XPS spectra of MoS_2–NiO-2.

are introduced into f-MoS_2 upon sonication.[42] MoS_2–NiO hybrids have been prepared by fixing the initial concentration of f-MoS_2 and varying the ratios of Ni precursors to f-MoS_2, thus giving the products of MoS_2–NiO-1, MoS_2–NiO-2 and MoS_2–NiO-3 with increasing NiO contents. The resultant MoS_2–NiO hybrids show three diffraction peaks at $2\theta = 37.6$, 43.8 and 62.4°, which can be assigned to the (110), (200) and (220) planes of bunsenite NiO (JCPDS card No. 47-1049), respectively. The MoS_2–NiO hybrids exhibit broadened peaks compared with neat NiO, which indicate smaller particle crystal sizes of NiO within MoS_2–NiO hybrids.[43]

The composition of MoS_2–NiO-2 is further confirmed by X-ray photoelectron spectroscopy (XPS) analysis (Fig. 2b–d and S5†). The MoS_2–NiO-2 sample contains the elements of Mo, S, Ni and O without detectable impurities, indicating the co-existence of f-MoS_2 and NiO in the hybrids (Fig. S5a, ESI†). The binding energy peaks at 234.8 and 231.7 eV of the high-resolution Mo 3d spectrum (Fig. 2b) can be attributed to Mo $3d_{3/2}$ and Mo $3d_{5/2}$ of Mo^{4+}, respectively, suggesting the dominance of Mo^{4+} in the MoS_2–NiO-2. Besides, the small peak at ~226 eV corresponds to the S 2s component of MoS_2.[44] In the high-resolution S 2p spectrum (Fig. 2c), the peaks located at 161.6 and 162.9 eV correspond to S $2p_{1/2}$ and S $2p_{3/2}$ orbitals of divalent sulfide ions (S^{2-}) of f-MoS_2, respectively. Fig. 2d and S5b† show the high-resolution Ni 2p and O 1s spectra of the MoS_2–NiO-2 sample, respectively. Focusing on the Ni $2p_{3/2}$ state, the peaks can be separated into three peaks. The first peak centered at a binding energy of 853.5 eV corresponds to Ni^{2+} in the standard Ni–O octahedral bonding configuration in cubic NiO.[45,46] The second peak located at 855.0 eV can be assigned to the vacancy-induced Ni^{3+} ion[47] or Ni–OH bonds.[48] The third broad peak centered at 860.6 eV can be ascribed to a satellite peak in the NiO structure. Therefore, the Ni-related crystallite among the MoS_2–NiO-2 is mainly bunsenite NiO, and a small amount of the NiOOH phase is probably attached on the surface of NiO. These results clearly demonstrate the successful decoration of NiO on the f-MoS_2 nanosheets.

The morphologies of f-MoS_2 and MoS_2–NiO hybrids are further observed by field-emission scanning electron microscopy (FESEM). Fig. 3a shows that the f-MoS_2 nanosheets have a flat and smooth surface, and the lateral sizes of f-MoS_2 are in the range of several hundred nanometers, which is much smaller than those of b-MoS_2 (Fig. S6, ESI†). Transmission electron microscopy (TEM) images of f-MoS_2 (Fig. S7, ESI†) further demonstrate a nanosheet morphology. From Fig. S8a and b (ESI†), NiO nanosheets are sparsely interspersed on the surface of f-MoS_2 for MoS_2–NiO-1 when the initial mass ratio of $Ni(NO_3)_2$ to f-MoS_2 is 4 : 1. When the mass ratio of $Ni(NO_3)_2$ to f-MoS_2 increases to 8 : 1, the whole surface of f-MoS_2 is decorated with vertically aligned NiO nanosheet arrays (Fig. 3b and c), demonstrating a strong coupling effect between NiO and f-MoS_2. With a further increase in the initial mass ratio of $Ni(NO_3)_2$ to f-MoS_2, densely distributed and even seriously aggregated NiO nanosheets are observed on the f-MoS_2 templates (Fig. S8c and d, ESI†), indicating that here f-MoS_2 templates provide limited space for the further distribution of additional NiO nanosheets. For comparison, in the absence of a f-MoS_2 template, only densely accumulated layered NiO nanosheets are obtained under similar preparation conditions (Fig. S9, ESI†), demonstrating that f-MoS_2 templates efficiently prevent the severe aggregation of NiO themselves.

The TEM images of the MoS_2–NiO-2 are also shown in Fig. 3d. It can be distinctly seen that NiO nanosheets are uniformly confined on the surface of f-MoS_2, which keeps well with SEM observations. Fig. 3e shows the TEM image of MoS_2–NiO-2 taken from the sample edge, from which f-MoS_2 templates are closely immobilized with vertically aligned NiO nanosheet arrays. Fig. 3f shows a high-resolution TEM (HRTEM) image from the square area in Fig. 3e, revealing the lattice fringes with an interplanar spacing of 0.148 and 0.267 nm which are assigned to the (220) lattice planes of cubic NiO and (101) lattice planes of 2H-phase MoS_2, respectively. The corresponding TEM and SEM energy-dispersive spectra (EDS) elemental mappings are shown in Fig. 3g and S10,† respectively. The co-existence of uniform elemental distributions of Mo, S, Ni and O are found in the view of all areas, indicating an efficient hybridization of NiO and f-MoS_2. Compared with a particle-on-sheet configuration, the vertically aligned morphology of MoS_2–NiO hybrids guarantees strong interfacial interactions between 2D NiO and f-MoS_2.[49,50] Particularly, NiO not only acts as an energy storage reservoir but also boosts efficient electron injection from NiO to MoS_2 due to electronic couplings between Ni centers and n-type semiconductor f-MoS_2.[51] The morphological results further evidence the enlarged BET surface area of MoS_2–NiO hybrids compared with neat f-MoS_2 and NiO. Among all MoS_2–NiO hybrids, MoS_2–NiO-2 possesses the highest surface area with more linkage sites in van der Waals heterostructures, which not only prevents f-MoS_2 nanosheets from restacking but also endows more channels from electrolytes to the electrode matrix.

Remarkably, MoS_2–Co_3O_4 and MoS_2–Fe_2O_3 hybrids can be fabricated by simply using cobalt and iron ions as precursors, respectively. FESEM and TEM images of MoS_2–Co_3O_4 and MoS_2–Fe_2O_3 hybrids exhibit the efficient hybridization of MoS_2

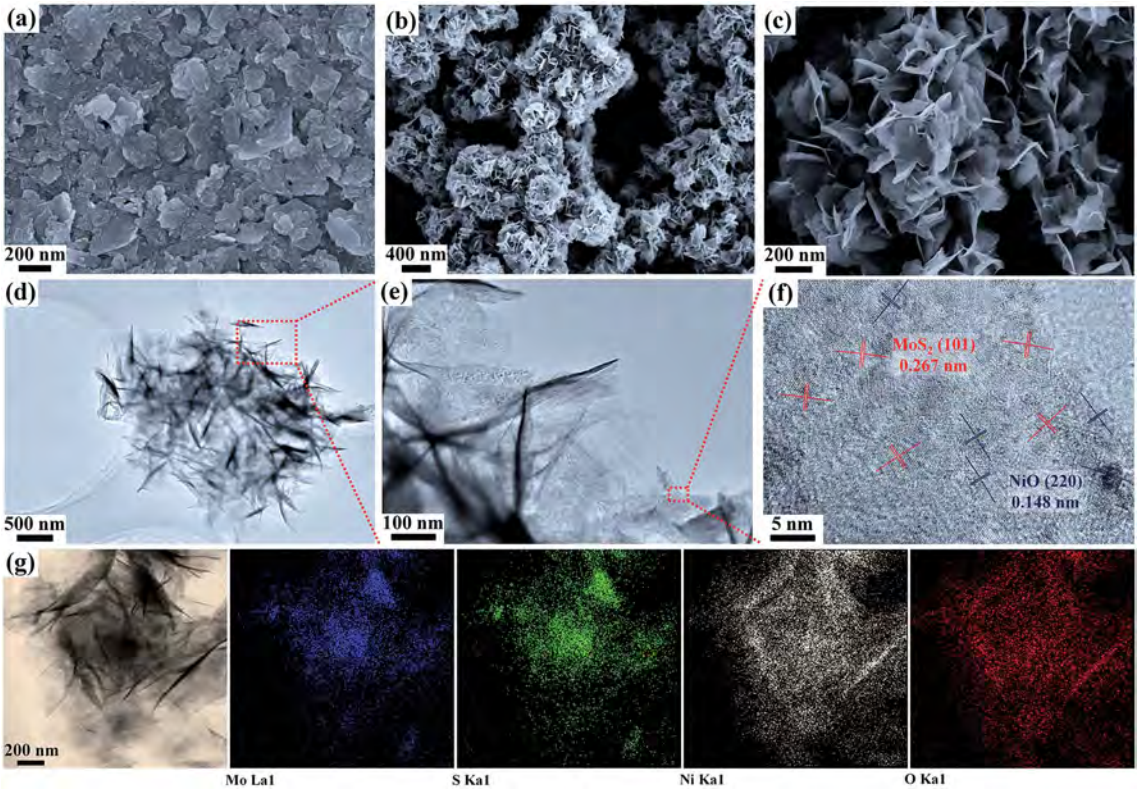

Fig. 3 FESEM images of (a) f-MoS_2 and (b and c) MoS_2–NiO-2. (d and e) TEM images of MoS_2–NiO-2 at low and high magnification. (f) HRTEM image of MoS_2–NiO-2. (g) Elemental mappings of MoS_2–NiO-2.

and porous transition-metal oxides (Fig. 4, S11 and S14, ESI†). For MoS_2–Co_3O_4 hybrids (Fig. 4a), Co_3O_4 nanowires are densely grown on 2D f-MoS_2, in which Co_3O_4 nanowire branches are connected with each other to form a framework structure. As shown in Fig. 4b and S11,† TEM images of MoS_2–Co_3O_4 indicate that 2D f-MoS_2 templates immobilize with Co_3O_4 nanowires (Fig. S12, ESI†) to form a porous network. In these gradually magnified TEM images (Fig. S11, ESI†), the f-MoS_2 templates act as the backbone materials, while the Co_3O_4 nanowires are rooted on the f-MoS_2 template. Fig. 4c shows a HRTEM image of MoS_2–Co_3O_4 taken from the square area in Fig. 4b, lattice fringes with a spacing distance of 0.241 and 0.62 nm

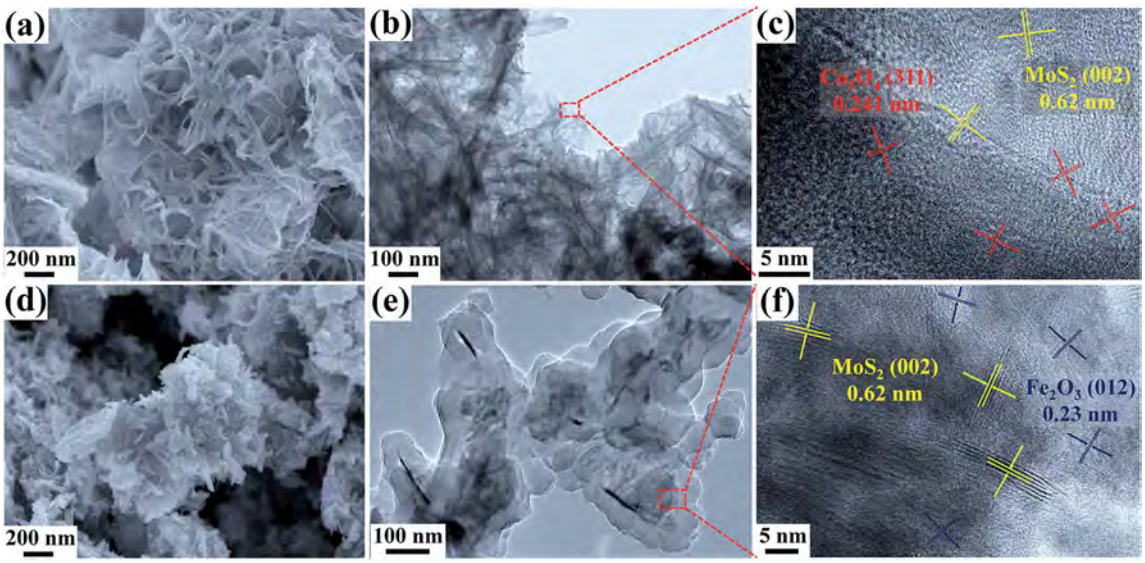

Fig. 4 FESEM, TEM and HRTEM images of (a–c) MoS_2–Co_3O_4 and (d–f) MoS_2–Fe_2O_3.

corresponding to the (311) planes of Co_3O_4 and (002) planes of MoS_2, respectively. Likewise, the morphology of MoS_2–Fe_2O_3 hybrids is revealed by the SEM and TEM observations (Fig. 4d–f). Particularly, Fig. 4d reveals that Fe_2O_3 nanoparticles (Fig. S15, ESI†) self-assemble into a nanorod structure when f-MoS_2 is integrated as templates. The nucleation and crystal growth of Fe_2O_3 on 2D MoS_2 can be described as a dissolution–recrystallization mechanism, in which the precursor particles gradually dissolve into the reaction solution and then the Fe_2O_3 nanorods are generated by an oriented attachment and Ostwald ripening mechanism.[52] TEM images of MoS_2–Fe_2O_3 (Fig. 4e and S14, ESI†) further demonstrate the uniform decoration of Fe_2O_3 nanorods on 2D f-MoS_2. Fig. 4f shows the HRTEM image of MoS_2–Fe_2O_3, indicating the clear lattice fringes with a lattice spacing of 0.23 and 0.63 nm, which corresponds to the (012) crystal plane of Fe_2O_3 and (002) crystal plane of MoS_2, respectively.

The unique structural features of the MoS_2–NiO hybrids are expected to be ideal for electrode materials due to their good structural stability, porous nanostructure, improved electrolyte/electrode contact and shortened electron/ion diffusion pathways. Electrochemical energy storage properties are investigated using MoS_2–NiO as electrode materials. Fig. 5a shows cycling voltammetry (CV) curves of f-MoS_2, MoS_2–NiO hybrids and NiO electrodes at a scan rate of 5 mV s^{-1}. The MoS_2–NiO-2 electrode exhibits the largest enclosed CV area, indicating that MoS_2–NiO-2 shows the best electrochemical capacitive performance among all the measured samples. The CV curves of f-MoS_2 show quasi-rectangular shapes without obvious redox peaks, indicating that the f-MoS_2 possesses a typical electrical double layer capacitance. A pair of well-defined cathodic and anodic peaks is clearly observed in the CV curves of MoS_2–NiO hybrids at ~0.46 and 0.29 V, respectively, which correspond to the faradaic redox reactions between NiO and NiOOH in an alkaline solution as follows:[53]

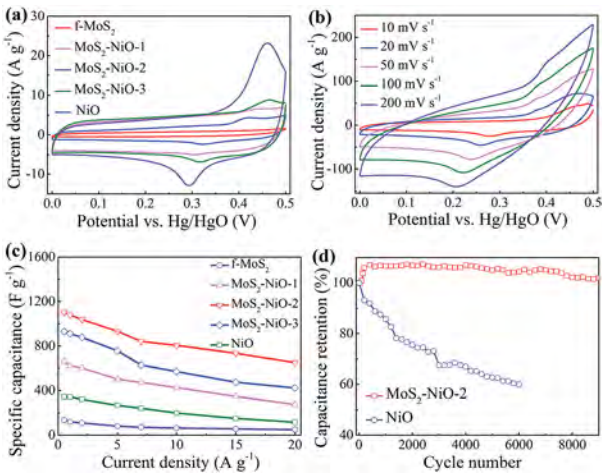

Fig. 5 (a) Comparison of CV curves of MoS_2–NiO, NiO and f-MoS_2 at 5 mV s^{-1}. (b) CV curves of MoS_2–NiO-2 at various scan rates. (c) Comparison of specific capacitances of MoS_2–NiO, NiO and f-MoS_2 at various current densities. (d) Cycling stability of MoS_2–NiO-2 and NiO at 2 A g^{-1}.

$$NiO + OH^- \leftrightarrow NiOOH + e^-$$

Fig. 5b shows CV curves of MoS_2–NiO-2 at different scan rates ranging from 10 to 200 mV s^{-1}. The shape of CV curves changes a little even at a fast scan rate of 200 mV s^{-1}, indicating fast electron/ion diffusion channels within the MoS_2–NiO-2 electrode. Notably, the CV curves of neat graphite paper and MoS_2–NiO-2 are illustrated in Fig. S17 (ESI†). The CV curve of a neat graphite paper electrode shows a rectangular shape with an ideal electrical double-layer capacitive behavior, but exhibits a much smaller surrounded area compared with that of MoS_2–NiO-2, indicating its nearly ignorable contribution when calculating the specific capacitance of the samples. Meanwhile, the cathodic peak current densities of MoS_2–NiO-2 and NiO electrodes are plotted (Fig. S18, ESI†) as functions of the square roots of scan rates ($v^{1/2}$), which are in accordance with the Cottrell equation and indicate a diffusion-controlled non-surface process.[54,55] Typically, the apparent diffusion coefficient (D) of OH^- ions in electrodes can be calculated by employing the Randles–Sevcik equation:[54]

$$I_p = 2.69 \times 10^5 \times n^{3/2} \times A \times \sqrt{D} \times C \times \sqrt{v}$$

where I_p is the peak current, n is the number of electrons involved in the redox reaction, A is the surface area of the electrode, D is the diffusion coefficient of the electrode material, C is the proton concentration, and v is the scan rate. According to the above formula, the diffusion coefficient of the MoS_2–NiO-2 electrode ($D_{MoS_2-NiO-2}$) is calculated to be ~13.8 times larger than that of the neat NiO electrode (D_{NiO}), indicating excellent ion mobility and remarkably better electrolyte penetration within the MoS_2–NiO-2 electrode:

$$\frac{D_{MoS_2-NiO-2}}{D_{NiO}} = \left(\frac{\left(\frac{I_p}{\sqrt{v}}\right)_{MoS_2-NiO-2}}{\left(\frac{I_p}{\sqrt{v}}\right)_{NiO}} \right)^2 = (17.1/4.6)^2 = 13.8$$

The relationships of specific capacitances as a function of current densities for all the samples are calculated and presented in Fig. 5c. The MoS_2–NiO-2 electrode exhibits the highest specific capacitance of ~1100 F g^{-1} at 0.5 A g^{-1}. The capacitance retains as high as 59% of its initial value at 0.5 A g^{-1} as the current density increases to 20 A g^{-1}, indicating an excellent rate capacitance retention. To advance the account of the enhanced capacitive activity of a MoS_2–NiO-2 hybrid, the electrochemical active surface area (ECSA) of the samples was estimated by measuring the double-layer capacitance (C_{dl}) accruing to the CV curves at different scan rates (Fig. S19, ESI†). Therefore, the ECSA value of MoS_2–NiO-2 is calculated to be 150.3 cm^2, which is much higher than that of neat MoS_2 (30.0 cm^2) and neat NiO (88.8 cm^2). Besides, the roughness factor (RF) is determined from the ratio of ECSA to the geometric area of the electrode, 1 cm^2. Hence, the RF values are estimated to be 150.3 (MoS_2–NiO-2), 30.0 (f-MoS_2) and 88.8 (NiO). As a result, the MoS_2–NiO-2 electrode has an ECSA nearly 5 times larger

than that of neat f-MoS_2 and 1.7 times larger than that of neat NiO, suggesting that the integration of f-MoS_2 and NiO can optimize the efficient surface area and endow more exposed active sites.

The specific capacitances of MoS_2–NiO-2 hybrids are larger than simple summations of neat NiO and f-MoS_2, which obviously resulted from the synergistic effect derived from the hybridization of 2D f-MoS_2 and NiO.[54] The combination of 2D f-MoS_2 and NiO into an integrated 3D architecture is responsible for improved charge transfer and decreased internal resistance. First, vertically aligned heterostructures of MoS_2–NiO hybrids provide atomically sharp interfaces with ultrafast charge transfer due to efficient electron–hole pair separation within MoS_2–TMO heterostructures,[56] and NiO nanosheet arrays provide efficient ion diffusion channels. Second, the unique 2D template, f-MoS_2, not only acts as electrochemically active materials with lower internal resistance (see EIS analysis and relative discussion in Fig. S22, ESI†), but also promotes the decoration of 2D NiO nanosheet arrays with sufficient nucleation sites for the growth of NiO,[54,57] and hence promotes efficient reversible redox reactions readily for enhanced electrochemical capacitive performances.[52] Compared with face-to-face stacked f-MoS_2 and NiO architectures in neat f-MoS_2 or NiO samples, the integration of f-MoS_2 and NiO can prevent the agglomeration of NiO nanosheets and the re-stacking of MoS_2 templates. On account of merits for the construction of MoS_2–NiO hybrids mentioned above, the specific capacitance of MoS_2–NiO-2 was carefully compared with those of NiO-based hybrids in other literatures (Table S2, ESI†). Our study thus makes an important breakthrough in the rational design and green fabrication of TMO-based electrode materials for supercapacitors.

To further evaluate the performances of the as-prepared MoS_2–NiO hybrids for practical applications, Fig. 5d illustrates the cycling stability of the MoS_2–NiO-2 electrode at a current density of 2 A g^{-1}. The capacitance retention of the MoS_2–NiO-2 electrode reaches ~101.9% of the initial capacitance after 9000 charge/discharge cycles, which is much better than that of the NiO electrode (below 60% capacitance retention after only 6000 cycles). The robustness of the interconnected network and the strong interfacial interaction between well-dispersed NiO and f-MoS_2 within nanosheet-on-nanosheet heterostructured MoS_2–NiO hybrids might be responsible for excellent electrochemical stability during cycling.[58]

We further investigate the electrochemical performance of MoS_2–Co_3O_4 and MoS_2–Fe_2O_3 in order to demonstrate the potential applications of such unique hybrid materials as electrode materials for supercapacitors. The pseudocapacitive behaviors of MoS_2–Co_3O_4 are evaluated by CV measurements at a scan rate of 5 mV s^{-1} in 6 M KOH electrolyte in the potential window of 0 to 0.55 V (*vs.* the Hg/HgO electrode), as shown in Fig. S23a (ESI†). For the MoS_2–Co_3O_4 electrode, its pseudocapacitive process is associated with a couple of redox peaks, which correspond to the reversible conversion reaction between CoOOH and Co_3O_4, illustrated as follows:

$$Co_3O_4 + OH^- + H_2O \leftrightarrow 3CoOOH + e^-$$

The specific capacitances of these electrodes at different current densities are plotted in Fig. S23c (ESI†). All the curves of the electrodes containing Co_3O_4 are not completely a straight line, indicating a pseudocapacitance behavior. The specific capacitance of MoS_2–Co_3O_4 at 1 A g^{-1} is calculated to be 1088.5 F g^{-1}. Significantly, the MoS_2–Co_3O_4 electrode still retains a capacitance as high as 1011.8 F g^{-1} even at 10 A g^{-1} while the specific capacitances of f-MoS_2 and Co_3O_4 electrodes are 196.4 F g^{-1} and 290.9 F g^{-1}, respectively, at the same current density. The cycling stability of the Co_3O_4 and MoS_2–Co_3O_4 electrodes is plotted in Fig. S23d (ESI†). The capacitance of MoS_2–Co_3O_4 retains more than 93% after 6000 charge/discharge cycles, demonstrating a largely improved cycling stability than that of neat Co_3O_4 (a capacitance retention of 51.6% after 6000 charge/discharge cycles). Likewise, the detailed electrochemical performances of MoS_2–Fe_2O_3 hybrids are also evaluated and detailed as discussed in Fig. S25 and S26 (ESI†).

It should be noted that the pseudocapacitive behaviors of MoS_2–Fe_2O_3 are stable and thus evaluated in 6 M KOH electrolyte in the potential window of −1.2 to 0 V (*vs.* the Hg/HgO electrode), which greatly provides the possibility of using such MoS_2–Fe_2O_3 as negative materials for asymmetric supercapacitors (ASCs). ASC devices are further assembled using MoS_2–NiO or MoS_2–Co_3O_4 hybrids as the positive electrode materials and MoS_2–Fe_2O_3 as the negative electrode material to boost the energy density of resultant ASC devices.

Fig. 6a shows the as-assembled ASC device with a MoS_2–NiO//MoS_2–Fe_2O_3 configuration lighting a red LED. Fig. 6b shows CV curves of the MoS_2–NiO//MoS_2–Fe_2O_3 ASC device with a voltage window of 0–2.0 V at 50 mV s^{-1}. The CV curves of the MoS_2–NiO//MoS_2–Fe_2O_3 ASC device remain stable without electrochemical water splitting when its potential window increases up to 2.0 V, and this value is nearly two times that of conventional symmetric supercapacitors with aqueous electrolytes. Moreover, the high voltage range is favorable for boosting the energy density of supercapacitors, and also it enables fewer devices in series to reach desired high output voltage.[59] As shown in Fig. 6c, the CV shapes for the MoS_2–NiO//MoS_2–Fe_2O_3 ASC device within the potential window of 0–1.8 V are well maintained, even at a high scan rate of 200 mV s^{-1}, demonstrating fast mass and electron transfer. Fig. 6d shows the galvanostatic charge/discharge test, which reveals its rapid *I*–*V* responses and good capacitive characteristics. Moreover, the energy and power densities are calculated based on the equations below and plotted as a Ragone diagram.

$$E = \frac{1}{2} C \Delta V^2$$

$$P = \frac{E}{\Delta t}$$

where C represents the specific capacitance of the ASC device, ΔV refers to the operating voltage window of the device, Δt is the discharge time, E is the energy density, and P is the power density.

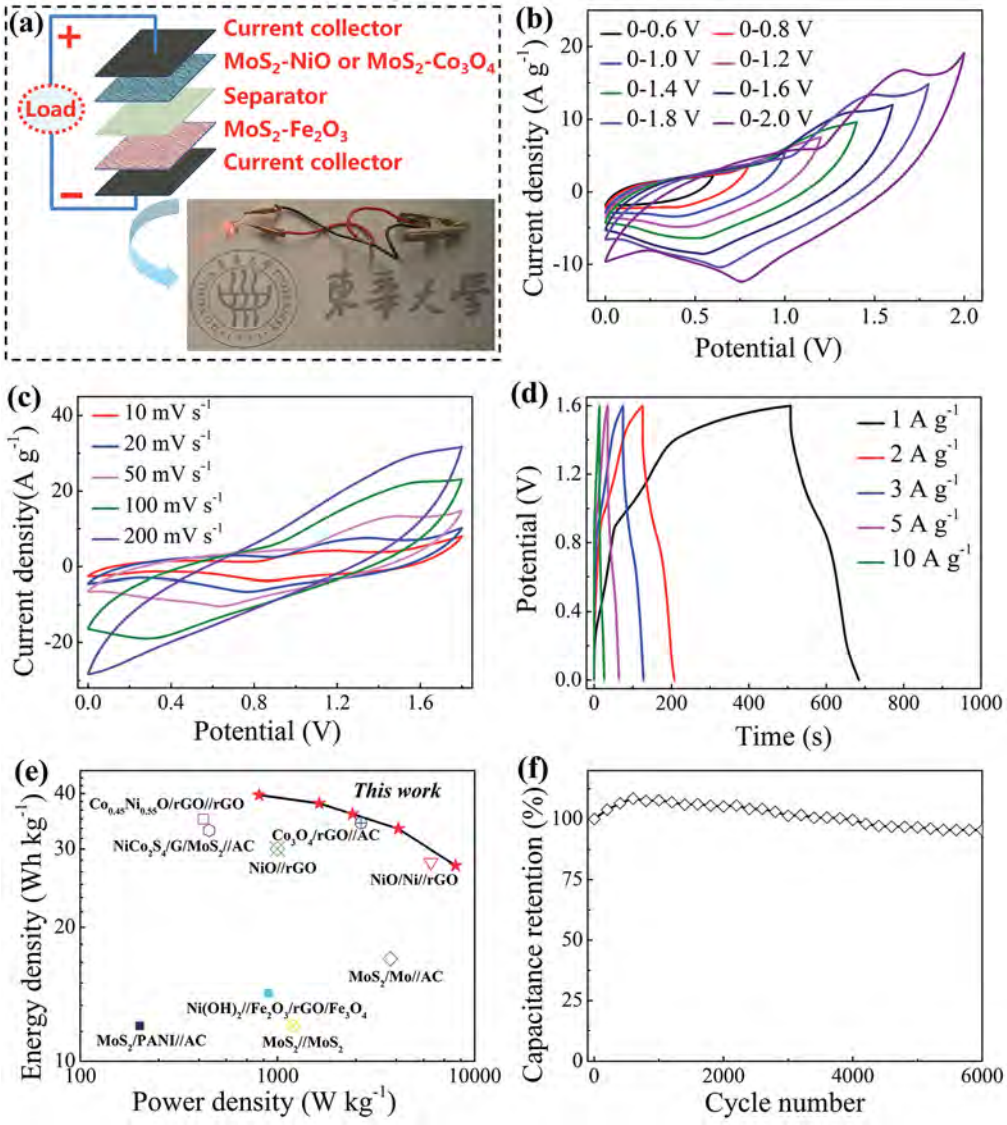

Fig. 6 Electrochemical performance of the assembled asymmetric supercapacitor. (a) The schematic illustration of the asymmetric supercapacitor fabrication and an LED indicator powered by the assembled device; (b and c) CV curves of the MoS_2–NiO-2//MoS_2–Fe_2O_3 asymmetric supercapacitor at different voltage windows and different scan rates; (d) the charge–discharge curves of the MoS_2–NiO-2//MoS_2–Fe_2O_3 device at different current densities; (e) Ragone plots of the MoS_2–NiO-2//MoS_2–Fe_2O_3 device compared to previous literatures; (f) cycling performance of the MoS_2–NiO-2//MoS_2–Fe_2O_3 asymmetric supercapacitor.

As displayed in Fig. 6e, the MoS_2–NiO-2//MoS_2–Fe_2O_3 ASC device shows a maximum energy density of 39.6 W h kg^{-1} at the power density of 807.2 W kg^{-1}, which is better than those of other previous literatures, such as NiO/Ni//activated carbon (30.12 W h kg^{-1} at 6080 W kg^{-1}),[56] NiO//rGO (30.3 W h kg^{-1} at 989 W kg^{-1}),[34] Co_3O_4/rGO//AC (34.3 W h kg^{-1} at 650 W kg^{-1}),[60] $Ni(OH)_2$//Fe_2O_3/graphene/Fe_3O_4 (14.2 W h kg^{-1} at 930 W kg^{-1}),[61] $Co_{0.45}Ni_{0.55}O$–rGO//rGO (35.1 W h kg^{-1} at 421 W kg^{-1}),[38] MoS_2//MoS_2 (14.2 W h kg^{-1} at 1200 W kg^{-1}),[62] MoS_2/Mo//AC (33.1 W h kg^{-1} at 743 W kg^{-1}),[63] MoS_2/PANI//AC (12.1 W h kg^{-1} at 200 W kg^{-1})[64] and $NiCo_2S_4$-g-MoS_2//AC (33.1 W h kg^{-1} at 450 W kg^{-1}).[65] The capacitance retentions of the MoS_2–NiO-2//MoS_2–Fe_2O_3 device as a function of charge/discharge cycles are displayed in Fig. 6f. The capacitance retention retains ~95% after 6000 charge/discharge cycles that identifies the good cycle life performance of such ASC devices.

Conclusions

In summary, we develop an extremely simple and scalable solvent-exchange method for the preparation of a high-concentration few-layered MoS_2 (f-MoS_2) suspension in water. Then a general formation of transition metal oxides (TMOs) such as NiO, Co_3O_4 and Fe_2O_3 on the large-surface area 2D f-MoS_2 substrates has been rationally designed and synthesized by a facile and cost-effective solution-processed strategy followed by a post annealing process. The resultant hetero-structured MoS_2–TMO hybrids show superior supercapacitive

performances compared with neat MoS_2 and TMOs, which might be ascribed to the atomically sharp interfaces among the heterostructured MoS_2–TMO hybrids providing ultrafast charge transfer, the greatly improved self-aggregation and synergistic effect between f-MoS_2 and TMOs, and the easy access of electrolyte ions to the electrode matrix due to the substantial intervals among the rationally designed heterostructures. Taking the MoS_2–NiO hybrid as an example, the vertically aligned heterostructured hybrids exhibit a high specific capacitance of 1121 F g^{-1} at a current density of 0.5 A g^{-1}, a good cycling stability (101.9% capacity retention after 9000 cycles at 2 A g^{-1}), and a remarkable rate capacitance (59% capacitance retention with the current density increasing from 1 to 20 A g^{-1}). This versatile synthetic method can be easily extended to fabricate other MoS_2–TMO heterostructures such as MoS_2–Co_3O_4 and MoS_2–Fe_2O_3 hybrids with excellent supercapacitive properties. The MoS_2–Co_3O_4 and MoS_2–Fe_2O_3 electrodes show 1088.5 and 647.8 F g^{-1}, respectively, at a current density of 1 A g^{-1}. A much improved cycling stability as well as excellent rate capacitance of the MoS_2–Co_3O_4 and MoS_2–Fe_2O_3 hybrids has also been observed. More importantly, the MoS_2–NiO-2//MoS_2–Fe_2O_3 asymmetric supercapacitor has been assembled, delivering a high energy density of 39.6 W h kg^{-1} at a power density of 807.2 W kg^{-1} and excellent cycling stability. We believe that the present method could be applicable for favorable and general contribution towards a simple and batch production of novel heterojunctioned functional MoS_2–based materials with great probability for various practical applications.

Acknowledgements

We are grateful for the financial support from the National Natural Science Foundation of China (21504012, 51125011, 51433001 and 21501091), the Fundamental Research Funds for the Central Universities (16D110617), the Program of Shanghai Subject Chief Scientist (17XD1400100) and the Natural Science Foundation of Shanghai (17ZR1439900).

Notes and references

1 R. B. Rakhi, W. Chen, D. Cha and H. N. Alshareef, *Nano Lett.*, 2012, **12**, 2559–2567.
2 F. Zhang, C. Yuan, J. Zhu, J. Wang, X. Zhang and X. W. Lou, *Adv. Funct. Mater.*, 2013, **23**, 3909–3915.
3 C. Xu, B. Xu, Y. Gu, Z. Xiong, J. Sun and X. S. Zhao, *Energy Environ. Sci.*, 2013, **6**, 1388–1414.
4 Z. Yu, L. Tetard, L. Zhai and J. Thomas, *Energy Environ. Sci.*, 2015, **8**, 702–730.
5 N. S. Choi, Z. Chen, S. A. Freunberger, X. Ji, Y. K. Sun, K. Amine, G. Yushin, L. F. Nazar, J. Cho and P. G. Bruce, *Angew. Chem., Int. Ed.*, 2012, **51**, 9994–10024.
6 Z. S. Wu, D. W. Wang, W. Ren, J. Zhao, G. Zhou, F. Li and H. M. Cheng, *Adv. Funct. Mater.*, 2010, **20**, 3595–3602.
7 R. B. Rakhi, W. Chen, M. N. Hedhili, D. Cha and H. N. Alshareef, *ACS Appl. Mater. Interfaces*, 2014, **6**, 4196–4206.
8 Q. Guan, J. Cheng, B. Wang, W. Ni, G. Gu, X. Li, L. Huang, G. Yang and F. Nie, *ACS Appl. Mater. Interfaces*, 2014, **6**, 7626–7632.
9 S. Gao, Y. Sun, F. Lei, L. Liang, J. Liu, W. Bi, B. Pan and Y. Xie, *Angew. Chem., Int. Ed.*, 2014, **53**, 12789–12793.
10 C. C. Hu, J. C. Chen and K. H. Chang, *J. Power Sources*, 2013, **221**, 128–133.
11 X. Wu, Z. Han, X. Zheng, S. Yao, X. Yang and T. Zhai, *Nano Energy*, 2017, **31**, 410–417.
12 T. Zhu, E. R. Koo and G. W. Ho, *RSC Adv.*, 2015, **5**, 1697–1704.
13 W. Zeng, L. Wang, H. Shi, G. Zhang, K. Zhang, H. Zhang, F. Gong, T. Wang and H. Duan, *J. Mater. Chem.*, 2016, **4**, 8233–8241.
14 M. G. Jeong, Z. Kai, S. Cherevko, W. J. Kim and C. H. Chung, *J. Power Sources*, 2013, **244**, 806–811.
15 F. Su, X. Lv and M. Miao, *Small*, 2015, **11**, 854–861.
16 C. Zhang, M. Antonietti and T. P. Fellinger, *Adv. Funct. Mater.*, 2014, **100**, 518–540.
17 H. Yi, H. Wang, Y. Jing, T. Peng and X. Wang, *J. Power Sources*, 2015, **285**, 281–290.
18 L. Li, K. Wang, Z. Huang, C. Zhang and T. Liu, *Nano Res.*, 2016, **9**, 2938–2949.
19 L. Li, H. Yang, J. Yang, L. Zhang, J. Miao, Y. Zhang, C. Sun, W. Huang, X. Dong and B. Liu, *J. Mater. Chem.*, 2016, **4**, 1319–1325.
20 Y. X. Zhang, X. Guo, X. Zhai, Y. M. Yan and K. N. Sun, *J. Mater. Chem.*, 2015, **3**, 1761–1768.
21 W. P. Jin, W. Na and J. Jang, *J. Mater. Chem.*, 2016, **4**, 8263–8271.
22 R. J. Zou, M. F. Yuen, Z. Y. Zhang, J. Q. Hu and W. J. Zhang, *J. Mater. Chem.*, 2015, **3**, 1717–1723.
23 A. K. Geim and I. V. Grigorieva, *Nature*, 2013, **499**, 419–425.
24 R. Wang and X. Yan, *Sci. Rep.*, 2014, **4**, 3712.
25 D. P. Dubal, D. Aradilla, G. Bidan, P. Gentile, T. J. Schubert, J. Wimberg, S. Sadki and P. Gomez-Romero, *Sci. Rep.*, 2015, **5**, 9771.
26 M. Long, E. Liu, P. Wang, A. Gao, H. Xia, W. Luo, B. Wang, J. Zeng, Y. Fu, K. Xu, W. Zhou, Y. Lv, S. Yao, M. Lu, Y. Chen, Z. Ni, Y. You, X. Zhang, S. Qin, Y. Shi, W. Hu, D. Xing and F. Miao, *Nano Lett.*, 2016, **16**, 2254–2259.
27 Y. Gao, Q. Liu and B. Xu, *ACS Nano*, 2016, **10**, 5431–5439.
28 M. Chhowalla and G. A. Amaratunga, *Nature*, 2000, **407**, 164–167.
29 T. Zhu, L. Zhu, J. Wang and G. W. Ho, *ACS Appl. Mater. Interfaces*, 2016, **8**, 32901–32909.
30 T. Zhu, J. Wang and G. W. Ho, *Nano Energy*, 2015, **18**, 273–282.
31 A. O'Neill, U. Khan and J. N. Coleman, *Chem. Mater.*, 2012, **24**, 2414–2421.
32 X. Cui, G. H. Lee, Y. D. Kim, G. Arefe, P. Y. Huang, C. H. Lee, D. A. Chenet, X. Zhang, L. Wang and F. Ye, *Nat. Nanotechnol.*, 2015, **10**, 534–540.
33 S. Saha, M. Jana, P. Khanra, P. Samanta, H. Y. Koo, N. C. Murmu and T. Kuila, *RSC Adv.*, 2015, **6**, 1380–1387.
34 L. Q. Mai, F. Yang, Y. L. Zhao, X. Xu, L. Xu and Y. Z. Luo, *Nat. Commun.*, 2011, **2**, 503–507.
35 J. Bae, M. K. Song, Y. J. Park, J. M. Kim, M. L. Liu and Z. L. Wang, *Angew. Chem., Int. Ed.*, 2011, **50**, 1683–1687.

36 K. Krishnamoorthy, G. K. Veerasubramani, P. Pazhamalai and S. J. Kim, *Electrochim. Acta*, 2016, **190**, 305–312.
37 X. Hong, J. Kim, S. F. Shi, Y. Zhang, C. Jin, Y. Sun, S. Tongay, J. Wu, Y. Zhang and F. Wang, *Nat. Nanotechnol.*, 2014, **9**, 682–686.
38 F. Luan, G. Wang, Y. Ling, X. Lu, H. Wang, Y. Tong, X.-X. Liu and Y. Li, *Nanoscale*, 2013, **5**, 7984–7990.
39 C. Backes, N. C. Berner, X. Chen, P. Lafargue, P. LaPlace, M. Freeley, G. S. Duesberg, J. N. Coleman and A. R. McDonald, *Angew. Chem., Int. Ed.*, 2015, **54**, 2638–2642.
40 J. N. Coleman, M. Lotya, A. O'Neill, S. D. Bergin, P. J. King, U. Khan, K. Young, A. Gaucher, S. De, R. J. Smith, I. V. Shvets, S. K. Arora, G. Stanton, H. Y. Kim, K. Lee, G. T. Kim, G. S. Duesberg, T. Hallam, J. J. Boland, J. J. Wang, J. F. Donegan, J. C. Grunlan, G. Moriarty, A. Shmeliov, R. J. Nicholls, J. M. Perkins, E. M. Grieveson, K. Theuwissen, D. W. McComb, P. D. Nellist and V. Nicolosi, *Science*, 2011, **331**, 568–571.
41 M. Yi, Z. G. Shen, S. S. Liang, L. Liu, X. J. Zhang and S. L. Ma, *Chem. Commun.*, 2013, **49**, 11059–11061.
42 U. Maitra, H. Matte, P. Kumar and C. N. R. Rao, *Chimia*, 2012, **66**, 941–948.
43 N. Mitoma, R. Nouchi and K. Tanigaki, *J. Phys. Chem. C*, 2013, **117**, 1453–1456.
44 J. Xie, H. Zhang, S. Li, R. Wang, X. Sun, M. Zhou, J. Zhou, X. W. Lou and Y. Xie, *Adv. Mater.*, 2013, **25**, 5807–5813.
45 S. S. Ji, Z. Yang, C. Zhang, Z. Y. Liu, W. W. Tjiu, I. Y. Phang, Z. Zhang, J. S. Pan and T. X. Liu, *Electrochim. Acta*, 2013, **109**, 269–275.
46 D. Liang, Z. Tian, J. Liu, Y. Ye, S. Wu, Y. Cai and C. Liang, *Electrochim. Acta*, 2015, **182**, 376–382.
47 Y. Shi, Y. Wang, J. I. Wong, A. Y. Tan, C. L. Hsu, L. J. Li, Y. C. Lu and H. Y. Yang, *Sci. Rep.*, 2013, **3**, 2169.
48 B. Sasi and K. G. Gopchandran, *Nanotechnology*, 2007, **18**, 1691.
49 K. L. Nardi, N. Y. Yang, C. F. Dickens, A. L. Strickler and S. F. Bent, *Adv. Energy Mater.*, 2015, **5**, 1500412.
50 X. Sun, G. Wang, J. Y. Hwang and J. Lian, *J. Mater. Chem.*, 2011, **21**, 16581–16588.
51 N. Kurra, N. A. Alhebshi and H. N. Alshareef, *Adv. Energy Mater.*, 2015, **5**, 1401303.
52 Y. Shuhua, S. Xuefeng, Z. Peng, S. Jing and G. Lian, *Small*, 2014, **10**, 2270–2279.
53 M. Srivastava, J. Singh, T. Kuila, R. K. Layek, N. H. Kim and J. H. Lee, *Nanoscale*, 2015, **7**, 4820–4868.
54 S. Liu, K. S. Hui and K. N. Hui, *ACS Appl. Mater. Interfaces*, 2016, **8**, 3258–3267.
55 Y. Du, L. Yang, J. Zhang, H. Liu, K. Majumdar, P. D. Kirsch and P. D. Ye, *IEEE Electron Device Lett.*, 2014, **35**, 599–601.
56 R. Long and O. V. Prezhdo, *Nano Lett.*, 2016, **16**, 1996–2003.
57 L. Ren, K. S. Hui and K. N. Hui, *J. Mater. Chem.*, 2013, **1**, 5689–5694.
58 H. Niu, X. Yang, H. Jiang, D. Zhou, X. Li, T. Zhang, J. Liu, Q. Wang and F. Qu, *J. Mater. Chem.*, 2015, **3**, 24082–24094.
59 Q. Wang, L. Jiao, H. Du, Y. Wang and H. Yuan, *J. Power Sources*, 2014, **245**, 101–106.
60 Q. Wang, X. Wang, B. Liu, G. Yu, X. Hou, D. Chen and G. Shen, *J. Mater. Chem.*, 2013, **1**, 2468–2473.
61 Q. Lu, M. W. Lattanzi, Y. Chen, X. Kou, W. Li, X. Fan, K. M. Unruh, J. G. Chen and J. Q. Xiao, *Angew. Chem., Int. Ed.*, 2011, **123**, 6979–6982.
62 L.-J. Xie, J.-F. Wu, C.-M. Chen, C.-M. Zhang, L. Wan, J.-L. Wang, Q.-Q. Kong, C.-X. Lv, K.-X. Li and G.-H. Sun, *J. Power Sources*, 2013, **242**, 148–156.
63 C. Zhao, X. Shao, Y. Zhang and X. Qian, *ACS Appl. Mater. Interfaces*, 2016, **8**, 30133–30142.
64 J. Ji, L. L. Zhang, H. Ji, Y. Li, X. Zhao, X. Bai, X. Fan, F. Zhang and R. S. Ruoff, *ACS Nano*, 2013, **7**, 6237–6243.
65 P. Ilanchezhiyan, G. M. Kumar and T. Kang, *J. Alloys Compd.*, 2015, **634**, 104–108.